A numerical study on gasification of a single-pore char particle in supercritical water

Chao Fan[1] · Hui Jin[1] · Yunan Chen[1] · Zhiwei Ge[1] · Qiuyang Zhao[1]

Abstract

Gasification models of a char particle based on the true porous structure are essential for the accurate simulation of gasifiers, and pore-scale study might provide important information for the development of the porous char particle gasification models. In this paper, a numerical study was conducted on the gasification of a single-pore char particle in supercritical water, and the emphasis was put on the gasification process inside the pore with the effects of surrounding fluid, pore structure and pore position considered. The results showed that the gasification in a pore was quite affected by pore diffusion. The increase in temperature and particle Reynolds number promoted the gasification in the pore, and convection mainly enhanced the heat transfer but had limited promotion on mass transfer in kinetically controlled regime. Increasing pore length and decreasing pore diameter caused the increase in diffusion resistance and the former had more obvious effects. However, the decreased pore diameter increased the specific surface area and benefited the whole char conversion. The pore position affected the species distribution inside the pore for non-diffusive gasification, and the impact was limited in kinetically controlled regime. Finally, study in this work will be further extended to the gasification of the porous char particle.

Keywords Supercritical water · Char gasification · Pore diffusion · Numerical simulation

Introduction

Coal is the main energy source and will continue to play an important role in next decades in China [1]. Currently, however, traditional coal utilization way of burning coal in a boiler has caused severe environmental problems such as high emission of gas pollutants, dust and carbon dioxide, and the efficiency is difficult to be further improved [2, 3]. Thus, seeking for a clean and efficient coal conversion way is of great significance.

Supercritical water gasification (SCWG) provides a promising option for the large-scale utilization of coal [4, 5]. In supercritical water (SCW), coal can be converted into hydrogen-rich gases efficiently, and pollutant elements are deposited and discharged in form of inorganic salts, owing to the excellent physical and chemical properties of SCW [6–8]. Besides, CO_2 can be enriched by means of pressure

regulation at the gasifier outlet [9]. Thus, this technology will have broad market prospect.

In research on SCWG, gasification behavior at the particle scale is the fundament of reaction-scale study. The gasification characteristics of solid particles can provide useful information for developing sub-models available in the design and optimization of gasifiers [10, 11]. Compared with traditional experimental methods, numerical simulation shows significant advantages that more gasification details can be revealed and good repeatability can be ensured [12–16], especially at the micron scale for particle research. In initial attempts on coal combustion/gasification simulation, coal particle was usually assumed to be nonporous dense sphere [17–19]. However, in the actual process, coal particles are typical porous media, especially for char particles after devolatilization [20]. To improve the model accuracy, porous assumption was adopted in later study. Richter et al. [21] studied the conversion behavior of a 200-µm spherical carbon particle in O_2/CO_2 atmosphere. Both cases with and without particle porosity considered were simulated, and the agreement of simulation results with experimental measurements was improved when the porous geometry was adopted. Xue et al. [22] conducted

✉ Hui Jin
   jinhui@mail.xjtu.edu.cn

[1] State Key Laboratory of Multiphase Flow in Power Engineering (SKLMF), Xi'an Jiaotong University, 28 Xianning West Road, Xi'an 710049, Shaanxi, China

numerical study on a single reacting porous char particle moving in O_2/CO_2 atmosphere, and the porosity was selected to be 0–0.4 by changing the pore structure. The calculated results showed that particles with higher porosity had higher sensitivity to the change of the O_2 concentration, and carbon consumption was found to be little affected by porosity in diffusion controlled regime. Fong et al. [23] reconstructed the 3D structure of a true char particle using micro-CT, and simulation was conducted on the gasification/combustion of the reconstructed char particle. Specifically, the work solved conservation equations based on first principles in large macropores and voids, while employed upscaled, effective-continuum equations in micro- and meso-pores.

Though extensive efforts have been made in traditional gasification and combustion areas, there are no relevant reports available on char gasification in SCW. Because of the unique physical and chemical properties of SCW, there might be quite differences for char particle gasification characteristics in conventional gasifying agents and SCW. Thus, the particle-scale study on char gasification in SCW is essential. Besides, in previous study, though porous characteristics of char particles were considered, focuses were still on the conversion of particle itself, and the detailed discussion on the process in a specific pore was still inadequate. Considering the above, this paper will carry out simulation on the gasification of a single-pore char particle in SCW, and the emphasis will be placed on the gasification process inside the pore. Effects of both surrounding fluid environment (temperature and convection) and pore itself (structure and position) will be taken into consideration and discussed.

Modeling

Physical model

The geometric model of the computational domain is shown in Fig. 1. A single-pore spherical char particle is placed in a fixed position in the flow field, and SCW flows around it to model the movement of the reacting char particle. To avoid blockage effects, the computational domain is selected to be large enough compared to the char particle, and its
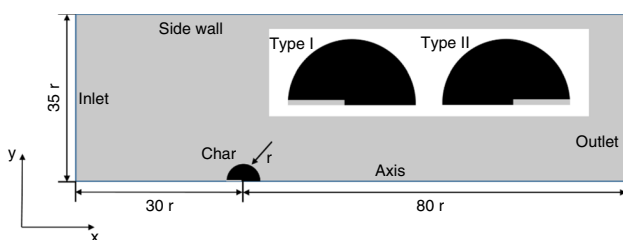

Fig. 1 Schematic diagram of the computational domain

size can be seen in Fig. 1. The particle radius is expressed as r, and d is the particle diameter which is selected to be 1 mm in this work. To save the computing resources, a two-dimensional axisymmetric model is used to replace the real three-dimensional process, and the effect of gravity is therefore neglected. Especially, the single pore is assumed to be cylindrical with an opening at one end, and the axis of the pore coincides with that of the overall geometric model. The pore length L_p ranges from 0.1 to 0.5 mm and pore diameter D_p ranges from 0.02 to 0.1 mm. Besides, two types of pores with opposite opening direction are selected to discuss the effect of pore position. For description convenience, the center of the spherical particle and the symmetry axis are, respectively, set as the coordinate origin and X axis in the two-dimensional coordinate system in Fig. 1.

The so-called pseudo-steady-state (PSS) approach [24, 25], which assumes the particle size does not change with time in the gasification process, is adopted in this work. The Stefan flow caused by char surface reactions is included in this model. The inflow SCW pressure is kept to be 25 MPa for all cases, and the inflow temperature T_{in} varies between 873 and 1023 K. The physical properties of SCW at a given temperature and pressure are calculated by IAPWS-IF97 [26]. The inlet in Fig. 1 is set to be velocity-inlet boundary, and the inflow velocity u_{in} is determined by the particle Reynolds number which is defined as:

$$\text{Re} = \frac{\rho_{in} u_{in} d}{\mu_{in}} \tag{1}$$

where ρ_{in} and μ_{in} are, respectively, the density and molecular viscosity of inflow SCW. The value of Re varies from 0 to 100, corresponding to the laminar flow area. Besides, the pressure-outlet and adiabatic boundary conditions are, respectively, selected for the outlet and side wall, and the slip wall is used for the side wall to ensure the inflow velocity to be uniform over the inlet cross section.

Governing equations

Based on the above assumptions, the mass and momentum conservation equations take the form:

$$\nabla \cdot (\rho u) = 0 \tag{2}$$

$$\nabla \cdot (\rho u u) = -\nabla P + \nabla \cdot (\tau) \tag{3}$$

where ρ, u, and P stand for the fluid density, flow velocity and static pressure, respectively. The stress tensor τ is given by

$$\tau = \mu \left[\left(\nabla u + (\nabla u)^T \right) - \frac{2}{3} \nabla \cdot u I \right] \tag{4}$$

with μ as the molecular viscosity and I as the unit tensor.

The energy conservation equation and species transport equation can be written as

$$\nabla \cdot (\rho u h) = \nabla \cdot (\lambda \nabla T - \sum_i h_i J_i) + S_h \tag{5}$$

$$\nabla \cdot (\rho u Y_i) = -\nabla \cdot J_i + R_i \tag{6}$$

where h and λ denote the enthalpy and thermal conductivity, respectively. It should be pointed out that, besides of the fluid, the heat conduction inside the char particle is also taken into account with the thermal conductivity of 129 W m^{-1} K^{-1}. J_i and Y_i stand for the diffusion flux and mass fraction, respectively, of species i. Fick's law is adopted for diffusion calculation, and the molecular diffusion coefficients are obtained from Ref. [27]. R_i is the net rate of production of species i by chemical reaction. S_h is the heat source term.

The $P-1$ radiation model is adopted in this work for the description of gas–gas radiation [28], which is written as

$$-\nabla q_r = \alpha G - 4\alpha n^2 \sigma T^4 \tag{7}$$

where q_r denotes the radiation heat flux, G is incident radiation, σ is the Stefan–Boltzmann constant, and T is the temperature. The absorption coefficient α for SCW is obtained form Ref. [29].
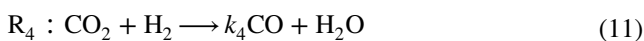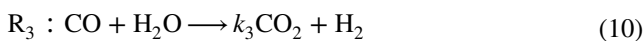
Reaction kinetics

In SCW, coal particles undergo devolatilization and char gasification processes, and the latter always consumes much more time than the former and is the rate-determining step of the whole process [30]. Therefore, only the char gasification step is considered in this work and the char particle is assumed to consist of carbon only. The following two heterogeneous reactions at char particle surface and two homogeneous reactions in the gas phase are considered in this model.

Fixed carbon reforming reaction:

$$R_1 : C + H_2O \longrightarrow k_1 CO + H_2 \tag{8}$$

$$R_2 : C + 2H_2O \longrightarrow k_2 CO_2 + 2H_2 \tag{9}$$
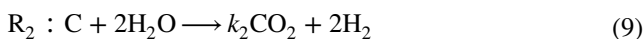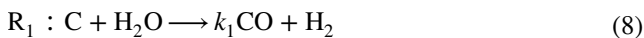
Water gas shift reaction:

$$R_3 : CO + H_2O \longrightarrow k_3 CO_2 + H_2 \tag{10}$$

$$R_4 : CO_2 + H_2 \longrightarrow k_4 CO + H_2O \tag{11}$$

The reaction rate constant k_i for reaction R_i is calculated using the Arrhenius equation:

$$k_i = A_i \exp\left(\frac{-E_{a,i}}{RT}\right) \tag{12}$$

where A_i and $E_{a,i}$ are, respectively, the pre-exponential factor and activation energy for reaction R_i. R is the universal gas constant. Kinetic parameters in this model are based on Su's work [31] and are listed in Table 1.

Discretization and numerical consideration

The computational domain was discretized by the finite volume method, and the commercial software ICEM CFD was used to generate structured grids. The grids near the particle surface were densified to obtain more accurate field distribution characteristics around the particle. The grid independence verification was also carried out using additional calculations with coarser and finer grids. The surface-averaged carbon consumption rate (both at outer surface $m_{c,o}$ and pore surface $m_{c,p}$) and surface-averaged temperature (both at outer surface $T_{s,o}$ and pore surface $T_{s,p}$) were used as the criterions, and their deviations were required to be less than 2% when the grid number doubled. Their definitions are as follows:

$$m_{c,j} = \frac{1}{A} \int \dot{m}_{c,j} \, dA \tag{13}$$

$$T_{s,j} = \frac{1}{A} \int \dot{T}_{s,j} dA \tag{14}$$

where $\dot{m}_{c,j}$ and $\dot{T}_{s,j}$ stand for the carbon consumption rate and surface temperature at the infinitesimal area of the selected area j (outer surface and pore surface), respectively, and A is the total area of the area j. Finally, 55,728 cells and 56,527 nodes were included in the model mesh.

The commercial software Fluent 18.2 was used to solve the problem described above. A double precision solver was adopted to improve convergence. The SIMPLE algorithm was used for pressure–velocity coupling, and the QUICK scheme was used for discretizing the convective terms.

Table 1 Kinetic parameters for heterogeneous and homogeneous reactions

Reactions	Rate constants	ln$A$	E_a/kJ mol^{-1}
R_1	k_1	-8.1678	27.76
R_2	k_2	12.3465	176.64
R_3	k_3	7.2192	96.83
R_4	k_4	11.2	133.06

Model validation

There are quite difficulties and uncertainties, such as variable measurement and experimental condition control, for the fine gasification or combustion experiments of a single char particle, especially in the high-pressure SCWG environment. Thus, the classic two-film model for diffusive combustion of a single spherical char particle in air was used for the model validation, and this approach was also used by other researches [32, 33] for combustion model validation. Although there are many differences between char gasification and combustion, they are both typical gas–solid reaction process, which is the strong coupling of heat transfer, mass transfer and chemical reactions. Therefore, the validation results of the combustion process will be used to evaluate the reliability of the gasification model here.

In the two-film model, two gas films, respectively, at the particle surface and the detached flame sheet are considered, and the reactions included are listed below. At the particle surface, carbon is oxidized to CO firstly (R_5), and CO is then oxidized to CO_2 at the detached flame sheet (R_6), which is assumed to be infinitely fast. The formed CO_2 diffuses to the particle surface and reacts with carbon to produce CO (R_7). When the process reaches the steady state, the mass fraction of O_2 and CO at the flame sheet is 0, and the temperature here is the highest. The details of this model can be found in Ref. [24].

$$R_5 : 2C + O_2 \rightarrow 2CO \tag{15}$$

$$R_6 : 2CO + O_2 \rightarrow 2CO_2 \tag{16}$$

$$R_7 : C + CO_2 \rightarrow 2CO \tag{17}$$

For calculation convenience, physical properties of all species were calculated as the function of inflow temperature T_{in} which varied from 1000 to 3000 K at intervals of 200 K, and the Lewis number (a dimensionless number defined as the ratio of thermal diffusivity to mass diffusivity) was set to be unity, for both the analytical codes and software cases. Radiation between particle surface and the ambient was considered, and the ambient temperature was taken from T_{in}. Two particle diameters of 1 and 0.1 mm were selected for consistency with gasification setting. The surface carbon consumption rate m_c, particle surface temperature T_s and flame sheet temperature T_f were chosen for comparison, and the calculated results are shown in Fig. 2. Good agreement between analytical and numerical results is observed, proving the numerical model is reliable.

Results and discussion

Effect of surrounding fluid

It is clear that the state of SCW around the char particle has direct influence on the gasification process. In this section, conditions of different inflow temperature T_{in} and particle Reynolds number Re were compared, and carbon consumption, temperature and species mole fraction characteristics are studied. Figure 3 shows the temperature field and species field distribution with varying T_{in} and Re. Both homogeneous and heterogeneous reactions caused non-uniform temperature field around the char particle, and the char surface temperature was obviously lower than surrounding fluid temperature because of the strongly endothermic surface reactions R_1 and R_2. With the increase in inflow temperature, gasification reactions were promoted, leading to the increase in temperature difference between main flow and char surface, while the increased Re reduced the temperature difference because of enhanced heat transfer. Different from the fluid phase, due to the stronger thermal conductivity ability of the char particle compared with the chemical reaction heat effect, the temperature gradient inside the particle was approximately zero, and the temperatures at the outer surface and pore surface were basically the same. Thus, the difference of surface gasification behavior inside and outside the pore only depended on the species concentration distribution. Besides, in the narrow and long semi-closed pore, the heat transfer with the external environment was weak, and the temperature field inside the pore was mainly determined by the fluid–solid coupled heat transfer. Thus, the temperature inside the pore was basically consistent with the char particle temperature, with only a tiny transition zone near the orifice to the external environment, as seen in Fig. 3.

Besides the wake thermal transfer with the external environment, the mass transfer was also limited inside the pore. It can be seen that the species mole fraction gradients inside the pore were obviously larger than that outside the pore. The SCW mole fraction near the outer surface was near 1, while the value inside the pore decreased significantly as the pore depth increased. Therefore, reactions on the outer char surface were obviously in kinetically controlled regime, while the gasification on the pore surface was significantly affected by pore diffusion. Meanwhile, the produced gases were also difficult to diffuse out of the pore. As there is an increase in T_{in} and Re, the temperature inside the pore increased, and reactions R_2 and R_3 were greatly promoted; thus more CO_2 and H_2 were produced and their mole fractions obviously increased, as seen in Fig. 3. Moreover, though more H_2 was produced than CO_2, the H_2 diffusion coefficient was larger than CO_2 diffusion

Fig. 2 Surface carbon consumption rate (**a**, **b**), particle surface temperature (**c**, **d**) and flame sheet temperature (**e**, **f**) as a function of inflow temperature for char particles with diameter of 1 mm (**a**, **c**, **e**) and 0.1 mm (**b**, **d**, **f**)
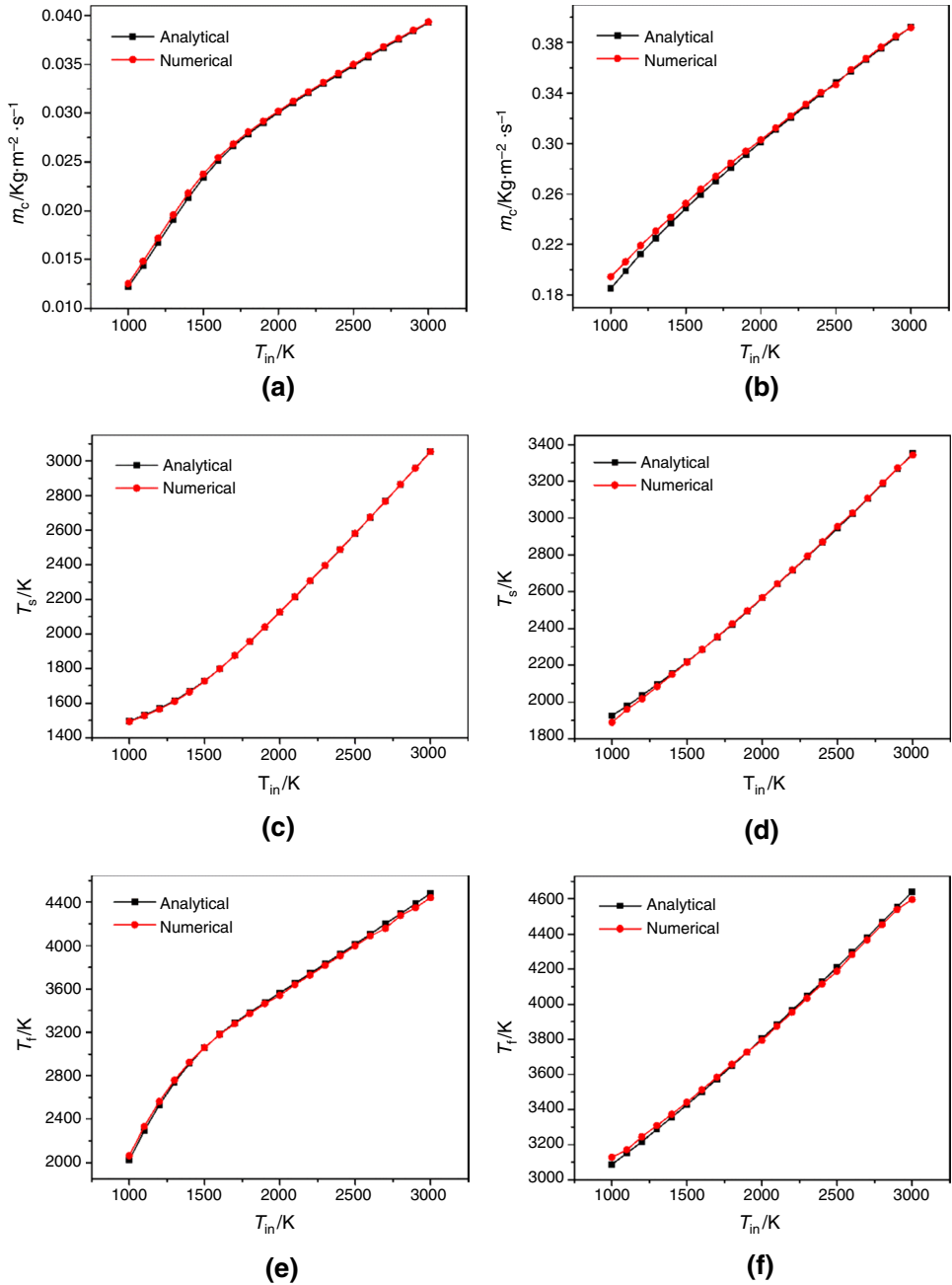
coefficient in SCW [27, 34]; thus the mole fraction of H_2 was less than that of CO_2 in the pore. For the species CO, because reactions R_1 and R_4 were not sensitive to temperature variation, its production increased slowly and the mole fraction decreased with T_{in} and Re.

Subsequently, the quantitative results will be discussed here. Figure 4a shows the surface-averaged carbon consumption rate of pore surface and its comparison with that of the outer surface using the ratio of $m_{c,o}$ to $m_{c,p}$. The possible factors influencing the char conversion inside the pore are displayed in Fig. 4b. As expected, the pore surface temperature increased with the inflow temperature, and the carbon

consumption rate increased accordingly. But the higher carbon consumption rate meant faster consumption of SCW, and more gas molecules were produced which hindered the diffusion of SCW, finally resulting in the decrease in SCW mole fraction in the pore. For the outer char surface, however, reactions were in kinetically controlled regime and nearly not affected by mass transfer. Besides, as mentioned above, the temperature difference between the surfaces inside and outside the pore can be ignored. Therefore, with the increase in T_{in}, the value of $m_{c,o}/m_{c,p}$ increased obviously. Taking the diffusive gasification (Re = 0) as an example, when T_{in} increased from 873 to 1023 K, the pore
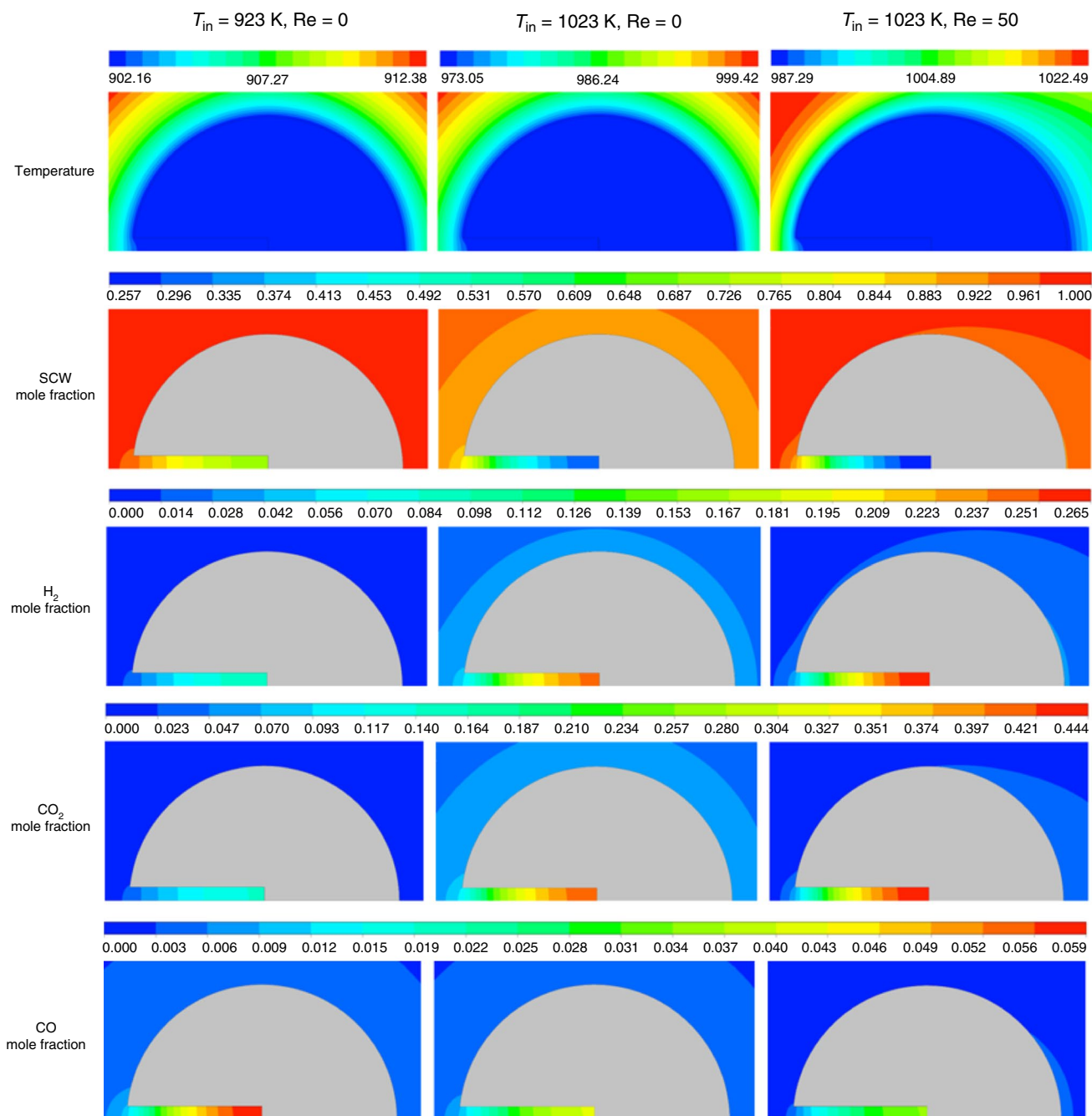
Fig. 3 Distribution of temperature field and species field at different inflow temperatures and particle Reynolds numbers ($L_p = 0.5$ mm, $D_p = 0.1$ mm)

surface temperature $T_{s,p}$ increased from 859.1 to 973.1 K and the average SCW mole fraction inside the pore, $Y_{SCW,p}$, decreased from 0.89 to 0.48, finally causing the increases of $m_{c,p}$ from 0.00042 to 0.0015 kg m^{-2} s^{-1} and $m_{c,o}/m_{c,p}$, from 1.14 to 2.01.

For the effect of convection, it can be seen in Fig. 4a that the carbon consumption rate at pore surface increased with particle Reynolds number. On the one hand, the convection

enhanced the heat transfer between the surrounding fluid and the char particle, causing the increase in char surface temperature, as seen in Fig. 4b, and the gasification was therefore promoted. On the other hand, the convection increased the SCW concentration and flow disturbance near the orifice, which enhanced the mass transfer of SCW into the pore, but the effects were very limited due to the semi-closed pore structure. It can be seen from Fig. 4b that the SCW mole
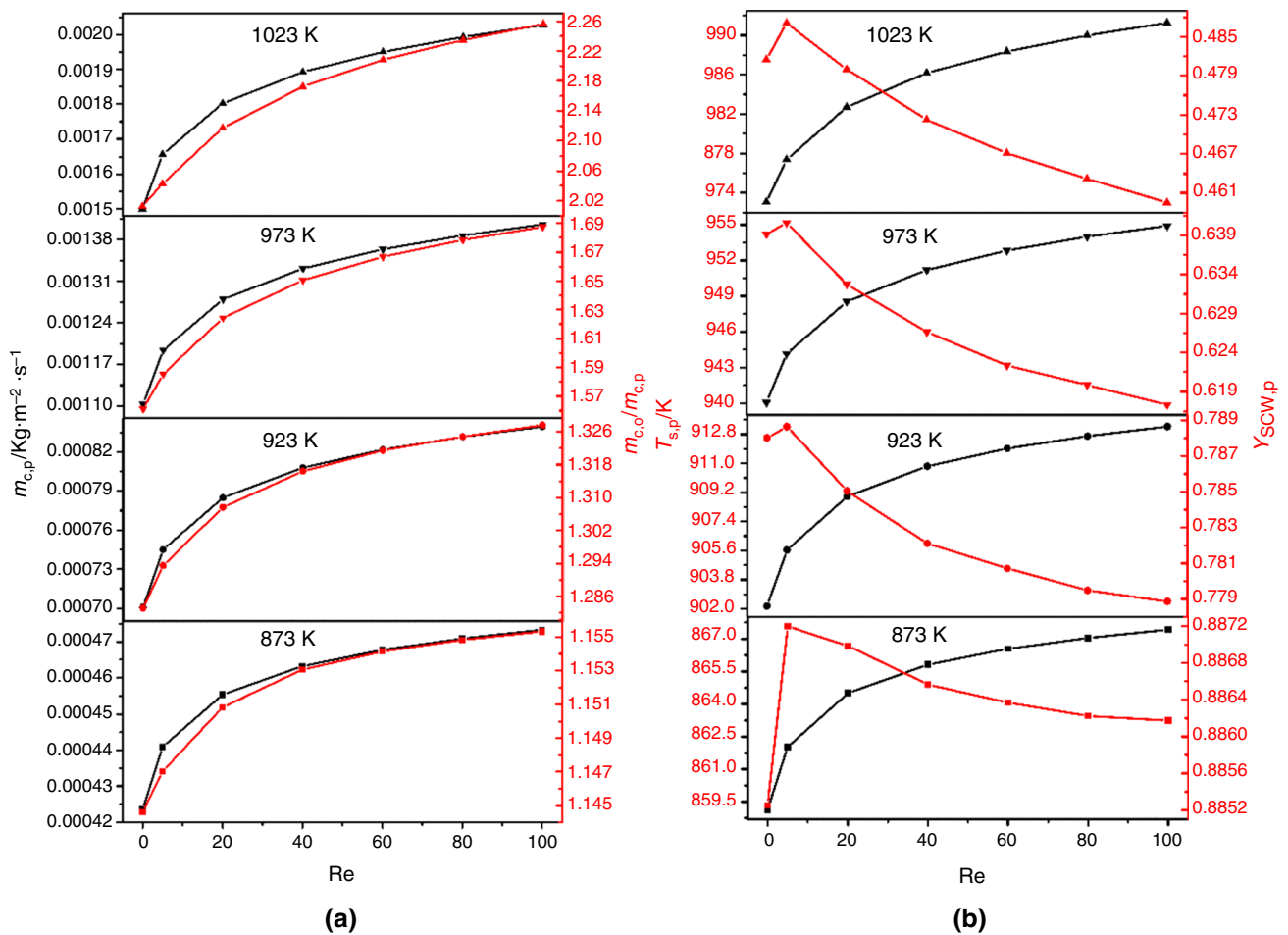
Fig. 4 Carbon consumption, pore surface temperature and SCW mole fraction inside the pore at different inflow temperatures and particle Reynolds numbers ($L_p = 0.5$ mm, $D_p = 0.1$ mm)

fraction inside the pore increased firstly, but then began to decrease with Re due to the faster SCW consumption at higher Re (higher $T_{s,p}$), which was also the reason why $m_{c,o}/m_{c,p}$ increased with Re. Therefore, it can be concluded that the increase in Re mainly contributed to heat transfer enhancement and less affected the mass transfer in the pore. With the increase in inflow temperature, the temperature difference between main flow and the char particle increased; thus the effects of convection became more obvious. For example, at T_{in} of 873 K and 1023 K, the Re increase from 0 to 100 raised $T_{s,p}$ by 8.3 K and 18.2 K, respectively, and promoted the carbon consumption inside the pore by 11.9–34.9%, respectively.

Effect of pore itself

In fact, the porous structure of coal particles is quite complex. Extensive studies have been carried out on the pore structure characteristics such as shape, size and its evolution in the reaction process [35–38]. For comprehensive

consideration of the model simplification, general applicability of the results and fluid continuity hypothesis, the micron-scale cylindrical pore was adopted, and discussions about pore length, pore diameter, pore scaling and pore position will be conducted as below.

Pore length

To investigate the effect of pore length, the pore diameter was fixed to be 0.1 mm, and the particle Reynolds number of 50 was selected for all cases. Figure 5 shows the carbon consumption at pore surface and its influencing factors. With the increase in L_p from 0.1 to 0.5 mm, $m_{c,p}$ decreased from 0.0040 to 0.0019 kg m^{-2} s^{-1}, by more than 50%. Because only a single pore was considered, the effect of pore structure changing on char particle temperature can nearly be neglected, as seen in Fig. 5 where the pore surface temperature difference caused by pore length changes was less than 0.5 K. Thus, the gasification inside a single pore was mainly affected by species distribution. As the L_p increases,
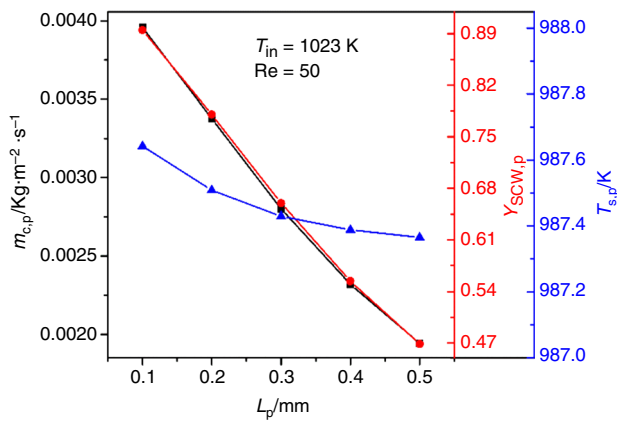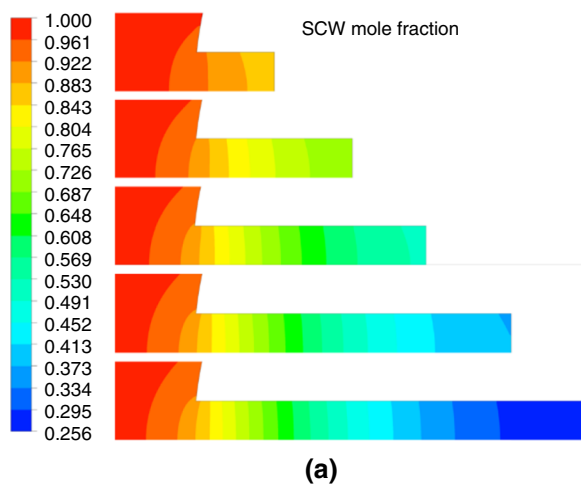
Fig. 5 Surface-averaged carbon consumption rate and temperature at pore surface and average SCW mole fraction inside the pore with different pore lengths

area, the carbon consumption at a certain pore surface position was reduced.

The effects of pore length at different temperatures were also compared as seen in Fig. 7. The ratio of carbon consumption rate $m_{c,o}/m_{c,p}$ was selected as the criteria because the gasification at the outer surface was scarcely affected by the single-pore structure changing. It can be seen that the pore length changing had more obvious impact on the gasification process at the higher temperature. When L_p increased from 0.1 to 0.5 mm, $m_{c,o}/m_{c,p}$ increased from 1.02 to 1.32 at 923 K, while from 1.08 to 2.19 at 1023 K. This was because the carbon consumption was faster at higher temperatures, making the gasification more determined by pore diffusion, and the effect of pore length changing was therefore amplified. This conclusion is also applicable to the variation of other pore structure parameters to be discussed later.
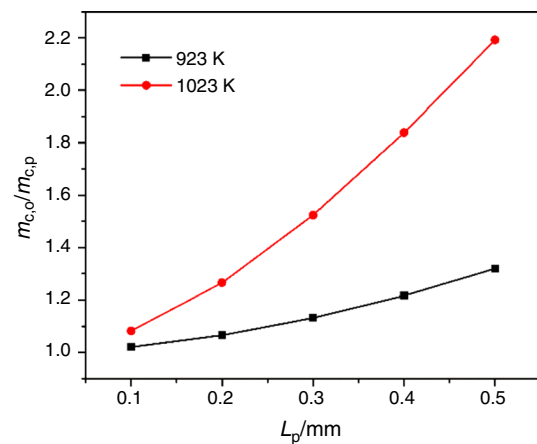
$Y_{SCW,p}$ decreased obviously due to the increased mass transfer resistance and showed the similar change trajectory with $m_{c,p}$. More details about SCW distribution in pores with different lengths are displayed in Fig. 6. SCW diffused into the pore and its concentration decreased along the diffusion direction as its continuous consumption. With the increase in L_p from 0.1 to 0.5 mm, the lowest SCW mole fraction in the pore decreased from 0.86 to 0.26. The maximum SCW concentration gradient inside the pore existed near the orifice, as seen in Fig. 6b, because of large diffusion resistance and relatively high gasification rate. Moreover, the species concentration at the same position for pores with different lengths also differed. The SCW mole fraction at a certain position was lower in a longer pore, and the larger slope meant the greater concentration gradient here. Thus, although the lengthened pore increased the reaction surface

Fig. 7 Carbon consumption comparison between pore and outer char surfaces with different pore lengths
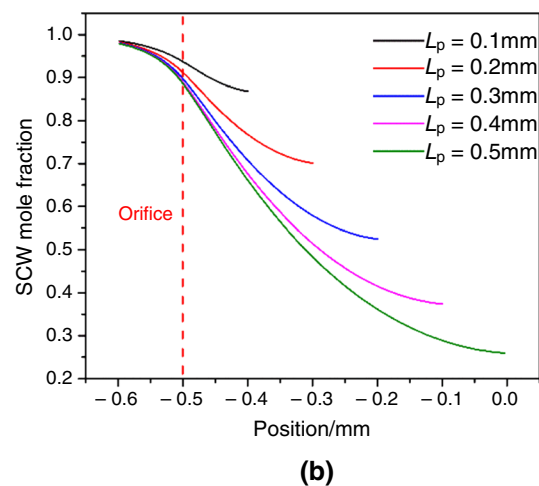

Fig. 6 Distributions of SCW mole fraction inside the pore (**a**) and along the pore axis (**b**) with different pore lengths at 1023 K
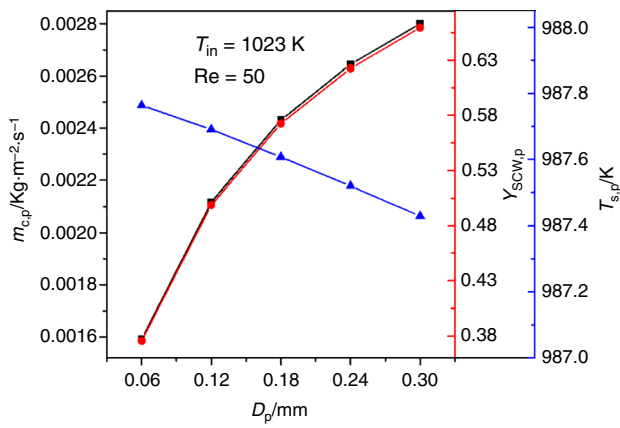
Fig. 8 Surface-averaged carbon consumption rate and temperature at pore surface and average SCW mole fraction inside the pore with different pore diameters
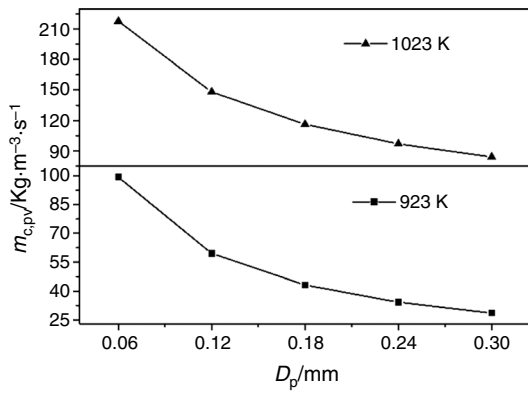

Fig. 9 Variation of volume-averaged carbon consumption rate with pore diameter

Pore diameter

The pore diameter variation will be discussed in this section, and the pore length and particle Reynolds number were, respectively, set to be 0.3 mm and 50. Taking the case where $T_{in} = 1023$ K as an example, a significant decrease in $m_{c,p}$ from 0.0028 to 0.0016 kg m^{-2} s^{-1} is observed in Fig. 8, when D_p decreased from 0.3 to 0.06 mm. Similar to the analysis of pore length, the pore diameter changing affected the species distribution obviously, while its effect on char particle temperature can nearly be ignored. With the decrease in D_p, the diffusion resistance increased, causing $Y_{SCW,p}$ to decrease from 0.66 to 0.38, with almost the same decline proportion of $m_{c,p}$. Furthermore, Fig. 9 displays the volume-averaged carbon consumption rate $m_{c,pv}$ in the pore, defined as the carbon consumption per unit pore volume per unit time. Although the small pore diameter led to the decline of $m_{c,p}$, significant increase in $m_{c,pv}$ was observed. When D_p decreased from 0.3 to 0.06 mm, $m_{c,pv}$ increased from 28.6 to 99.4 kg m^{-3} s^{-1} and from 84.0 to 217.8 kg m^{-2} s^{-1}, respectively, at 923 K and 1023 K. In summary, small pore diameters increased the pore diffusion resistance, but meanwhile, they increased the specific surface area and improve the space utilization efficiency, finally promoted the overall char particle gasification.

SCW distributions inside the pore and along the pore axis are shown in Fig. 10. It can be seen in Fig. 10a that the species field disturbance near the orifice caused by the existence of pore was reduced with smaller pore diameters. Correspondingly, in Fig. 10b, the SCW mole fraction in front of the orifice increased with the decrease in pore diameter. After diffusing into the pore, SCW mole fraction decreased sharply and dropped faster in pores with smaller pore diameters due to larger diffusion resistance in such pores. In Fig. 10b, the SCW mole fraction
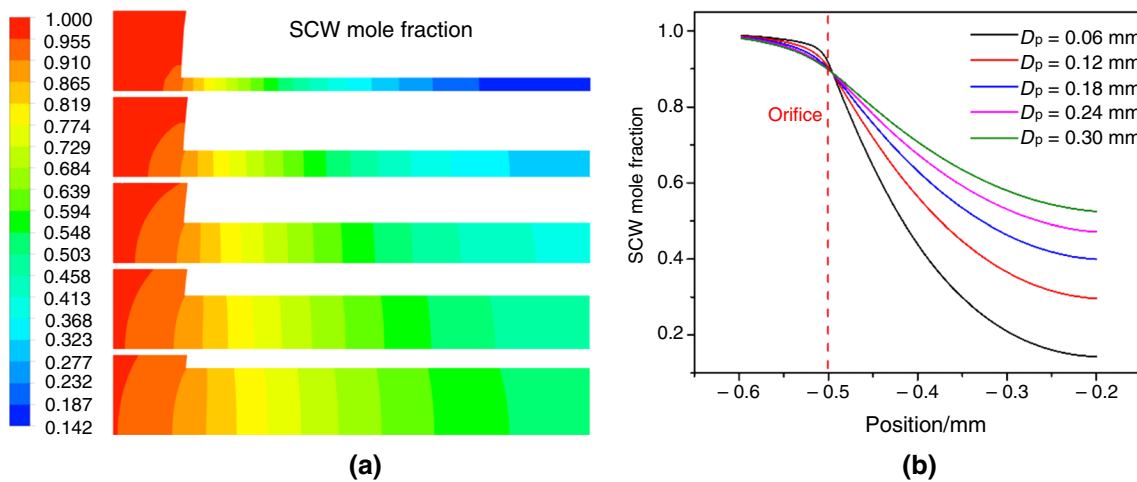

Fig. 10 Distributions of SCW mole fraction inside the pore (**a**) and along the pore axis (**b**) with different pore diameters at 1023 K

distribution curves intersected at a point near the orifice, after which the SCW mole fraction at the same position decreased with the decrease in the pore diameter and the difference between different pores increased at deeper position. Finally, the SCW mole fraction at the bottom of the pore decreased from 0.52 to 0.14 with pore diameter changing from 0.3 to 0.06 mm.

Pore scaling

Through the discussions above, both reducing pore diameter and increasing pore length will lead to the increase in diffusion resistance in the pore. In this section, the pore length and pore diameter were changed simultaneously, and its effect on the gasification in the pore will be studied. Based on the pore presented in Sect. 3.1 ($L_p = 0.5$ mm and $D_p = 0.1$ mm), pore sizes here were scaled with different scaling factors of 0.2–1, and the carbon consumption for these cases is shown in Fig. 11. When the pore length and pore diameter were reduced in the same proportion, the surface carbon consumption was promoted, indicating smaller mass transfer resistance in these pores. Taking the case where $T_{in} = 1023$ K and Re = 50 as an example, $m_{c,p}$ increased from 0.00194 to 0.00341 kg m^{-2} s^{-1}, by 75.8%, with the scaling factor changing from 1 to 0.2. From this point of view, the variation of pore length had more significant effect on gasification in the pore than that of pore diameter. Besides, for all conditions considered, $m_{c,o}/m_{c,p}$ had a good linear relationship with the scaling factor, with all correlation coefficient R^2 greater than 0.998. Because the effect of the single-pore structure on the carbon consumption on the outer char surface was negligible, it can be concluded that $1/m_{c,p}$ and the scaling factor were linearly related.

Pore position

For non-diffusive gasification process, field distributions at different positions around the char particle are quite different, especially at high Reynolds numbers, and gasification inside pores at different positions will therefore be affected. Considering the axisymmetric characteristic of 2D model in this work, two types of pores toward opposite direction (see Fig. 1) were selected for discussion, with the same pore length of 0.5 mm and pore diameter of 0.1 mm. Figure 12 shows the carbon consumption and SCW mole fraction in the pore. It can be seen that the carbon consumption inside the type I pore was faster than that inside the type II pore, due to higher SCW concentration in the type I pore. When SCW flowed around the char particle, produced gases on the upstream side of the particle can be easily taken away to maintain a higher SCW proportion, compared to the circumstance in the wake region where the environmental fluid was relatively stagnant, as seen in Fig. 13. And the higher SCW mole fraction around the orifice will lead to the same results inside the pore. Overall, the effect of pore position on char conversion was limited in this work because the gasification lied in the kinetically controlled region where the SCW concentration near the surface was close to saturation. The differences of $m_{c,p}$ caused by pore position changing did not exceed 6.8% in Fig. 12a.

Furthermore, from a more detailed analysis of the SCW distribution in the pore in Fig. 13, it can be seen that for both pores of type I and type II, the SCW mole fraction near the orifice increased with Re because of more efficient mass transfer around the outer char particle. After entering the pore, SCW was consumed faster at higher Re because of higher pore surface temperature as discussed in Sect. 3.1, finally SCW mole fraction began to decrease with Re at the same position of the pore. Comparing the two types of pore, it can be found that the SCW mole fraction inside the type
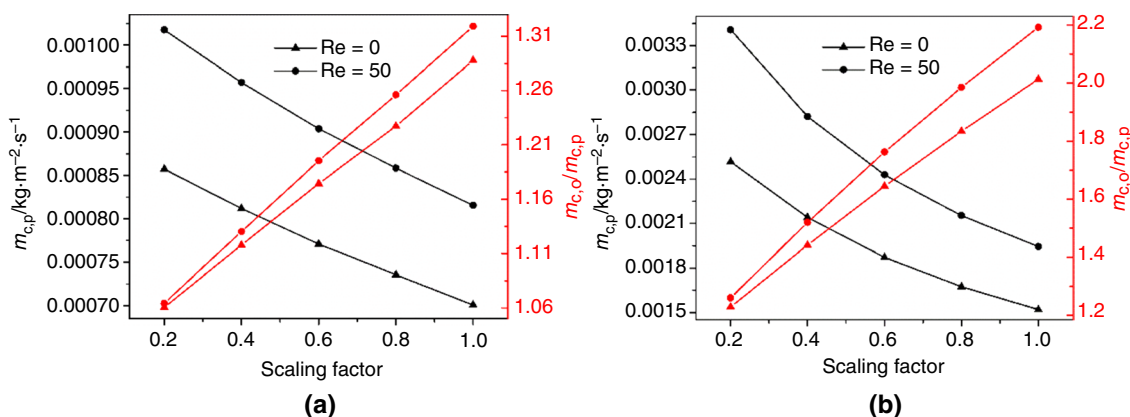

Fig. 11 Carbon consumption characteristics in pores with different sizes scaled based on L_p of 0.5 mm and D_p of 0.1 mm, at 923 K (**a**) and 1023 K (**b**)
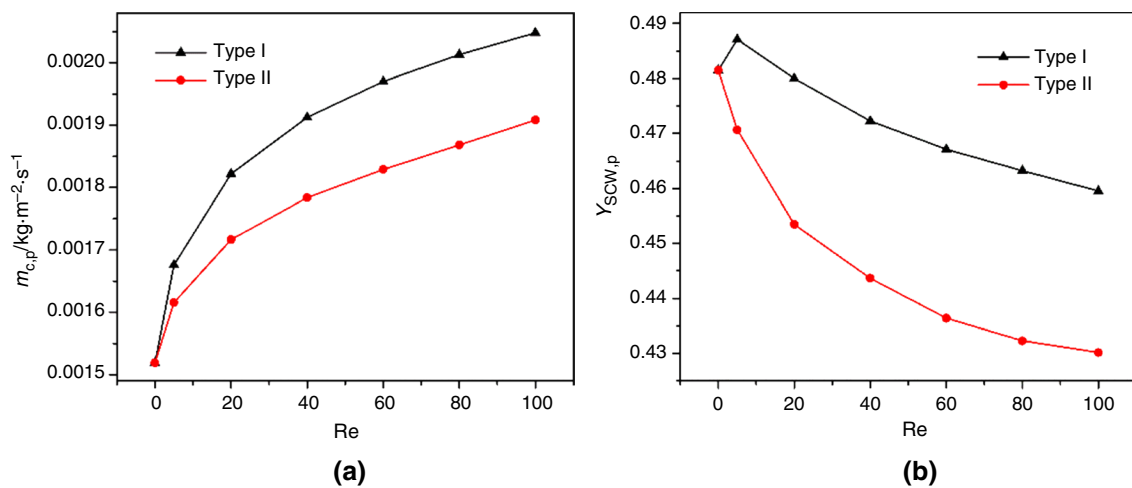
Fig. 12 Surface-averaged carbon consumption rate at pore surface (**a**) and average SCW mole fraction inside the pore (**b**) for pores toward opposite direction
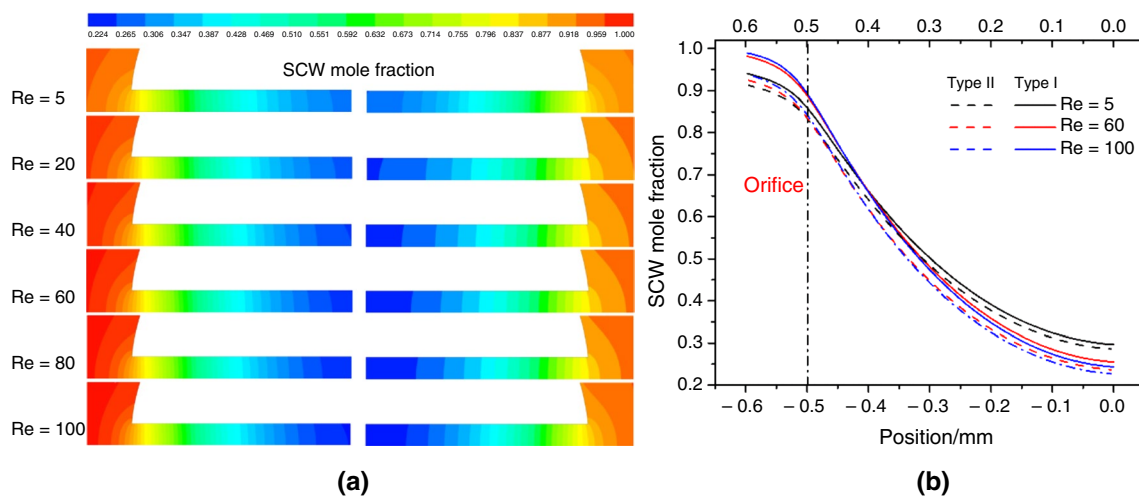

Fig. 13 Distributions of SCW mole fraction inside the pore (**a**) and along the pore axis (**b**) for pores toward opposite direction

I pore was always higher than that inside the type II pore at the same pore depth, as expected, and the difference was the largest at the orifice and decreased at deeper position of the pore. With Re of 100, for example, the SCW mole fraction difference between type I and type II pores was 0.051 at the orifice, and decreased to 0.016 at the bottom of the pore.

Conclusions

A numerical study was conducted in this work on the gasification of a single-pore char particle in supercritical water. The gasification process inside the pore was emphatically concerned with effects of environmental fluid (temperature and convection), pore structure (length, diameter) and pore position considered. The main conclusions can be obtained as follows:

1. Gasification inside the pore was more affected by mass transfer than that at outer char surface. The increase in temperature promoted the gasification and led to a lower SCW concentration in the pore. Convection promoted the gasification in the pore mainly by enhancing the heat transfer and had limited effect on the mass transfer in kinetically controlled regime.
2. The increase in pore length and decrease in pore diameter increased the mass transfer resistance, and the former had more obvious impact on char conversion. And the structure influences were amplified at higher temperatures. Besides, pores with small diameters increased

the specific surface area and benefited the whole char conversion.

3. The species distribution differed in pores at different positions for non-diffusive gasification, and this impact was limited in kinetically controlled regime due to nearly saturated SCW concentration near outer char surface.

Finally, information obtained in this work might be used to develop models for porous char particle gasification in SCW, further as sub-models that can be applied to reactor-scale simulation.

References

1. Zhao Y, Yang J, Ma S, Zhang S, Liu H, Gong B, et al. Emission controls of mercury and other trace elements during coal combustion in China: a review. Int Geol Rev. 2018;60(5–6):638–70.
2. Fan C, Jin H, Shang F, Feng H, Sun J. Study on the surface structure development of porous char particles in catalytic supercritical water gasification process. Fuel Process Technol. 2019;193:73–81. https://doi.org/10.1016/j.fuproc.2019.04.029.
3. Yuan J, Na C, Lei Q, Xiong M, Guo J, Hu Z. Coal use for power generation in China. Resour Conserv Recycl. 2018;129:443–53.
4. Jin H, Lu Y, Liao B, Guo L, Zhang X. Hydrogen production by coal gasification in supercritical water with a fluidized bed reactor. Int J Hydrog Energy. 2010;35(13):7151–60.
5. Bai B, Liu Y, Zhang H, Zhou F, Han X, Wang Q, et al. Experimental investigation on gasification characteristics of polyethylene terephthalate (PET) microplastics in supercritical water. Fuel. 2020;262:116630.
6. Guo L, Jin H, Lu Y. Supercritical water gasification research and development in China. J Supercrit Fluids. 2015;96:144–50.
7. Fan C, Guo S, Jin H. Numerical study on coal gasification in supercritical water fluidized bed and exploration of complete gasification under mild temperature conditions. Chem Eng Sci. 2019;206:134–45.
8. Bai B, Liu Y, Wang Q, Zou J, Zhang H, Jin H, et al. Experimental investigation on gasification characteristics of plastic wastes in supercritical water. Renew Energy. 2019;135:32–40.
9. Jin H, Fan C, Guo L, Liu S, Cao C, Wang R. Experimental study on hydrogen production by lignite gasification in supercritical water fluidized bed reactor using external recycle of liquid residual. Energy Convers Manag. 2017;145:214–9. https://doi.org/10.1016/j.enconman.2017.04.102.
10. Mermoud F, Golfier F, Salvador S, Van de Steene L, Dirion J-L. Experimental and numerical study of steam gasification of a single charcoal particle. Combust Flame. 2006;145(1–2):59–79.
11. Schulze S, Nikrityuk P, Compart F, Richter A, Meyer B. Particle-resolved numerical study of char conversion processes in packed beds. Fuel. 2017;207:655–62.
12. Xiong Q, Kong S-C. High-resolution particle-scale simulation of biomass pyrolysis. ACS Sustain Chem Eng. 2016;4(10):5456–61.
13. Bozorg MV, Doranehgard MH, Hong K, Xiong Q. CFD study of heat transfer and fluid flow in a parabolic trough solar receiver with internal annular porous structure and synthetic oil–Al$_2$O$_3$ nanofluid. Renew Energy. 2020;145:2598–614.
14. Ren F, Xiang L-K, Chu H-Q, Ya Y-C, Han W-W, Nie X-K. Numerical investigation on the effect of CO$_2$ and steam for the H$_2$ intermediate formation and NOX emission in laminar premixed methane/air flames. Int J Hydrog Energy. 2020;45:3785–94.
15. Izadi A, Siavashi M, Xiong Q. Impingement jet hydrogen, air and CuH$_2$O nanofluid cooling of a hot surface covered by porous media with non-uniform input jet velocity. Int J Hydrog Energy. 2019;44(30):15933–48.
16. Li D, Gao R, Dong L, Lam WK, Zhang F. A novel 3D re-entrant unit cell structure with negative Poisson's ratio and tunable stiffness. Smart Mater Struct. 2019. https://doi.org/10.1088/1361-665X/ab6696/meta.
17. Kestel M, Nikrityuk P, Hennig O, Hasse C. Numerical study of the partial oxidation of a coal particle in steam and dry air atmospheres. IMA J Appl Math. 2012;77(1):32–46.
18. Higuera F. Combustion of a coal char particle in a stream of dry gas. Combust Flame. 2008;152(1–2):230–44.
19. Ha MY, Choi BR. A numerical study on the combustion of a single carbon particle entrained in a steady flow. Combust Flame. 1994;97(1):1–16.
20. Jin H, Fan C, Guo L, Zhao X, Cao C, Wei W. Pore structure and its evolution in char during supercritical water gasification process. J Porous Med. 2019;22(2):195–207.
21. Richter A, Nikrityuk PA, Kestel M. Numerical investigation of a chemically reacting carbon particle moving in a hot O$_2$/CO$_2$ atmosphere. Ind Eng Chem Res. 2013;52(16):5815–24.
22. Xue Z, Guo Q, Gong Y, Xu J, Yu G. Numerical study of a reacting single coal char particle with different pore structures moving in a hot O2/CO2 atmosphere. Fuel. 2017;206:381–9.
23. Fong GH, Jorgensen S, Singer SL. Pore-resolving simulation of char particle gasification using micro-CT. Fuel. 2018;224:752–63.
24. Turns SR. An introduction to combustion. New York: McGraw-Hill; 1996.
25. Sundaresan S, Amundson NR. Diffusion and reaction in a stagnant boundary layer about a carbon particle. 5. Pseudo-steady-state structure and parameter sensitivity. Ind Eng Chem Fundam. 1980;19(4):344–51.
26. Wagner W, Cooper JR, Dittmann A, Kijima J, Kretzschmar H-J, Kruse A, et al. The IAPWS industrial formulation 1997 for the thermodynamic properties of water and steam. J Eng Gas Turbines Power. 2000;122(1):150–84. https://doi.org/10.1115/1.483186.
27. Zhao X, Jin H, Chen Y, Ge Z. Numerical study of H$_2$, CH$_4$, CO, O$_2$ and CO$_2$ diffusion in water near the critical point with molecular dynamics simulation. Comput Math Appl. 2019. https://doi.org/10.1016/j.camwa.2019.11.012.
28. Krishnamoorthy G, Rawat R, Smith PJ. Parallelization of the p-1 radiation model. Numer Heat Transf Part B Fundam. 2006;49(1):1–17.
29. Ren Z, Guo L, Jin H, Luo K (eds.). Integration of CFD codes and radiation model for supercritical water gasification of coal in fluidized bed reactor. In: International heat transfer conference digital library; 2018: Begel House Inc.
30. Gao X, Zhang Y, Li B, Zhao Y, Jiang B. Determination of the intrinsic reactivities for carbon dioxide gasification of rice husk chars through using random pore model. Biores Technol. 2016;218:1073–81.
31. Su X, Guo L, Jin H. Mathematical modeling for coal gasification kinetics in supercritical water. Energy Fuels. 2016;30(11):9028–35.
32. Kestel M, Nikrityuk P, Meyer B, (eds.). Numerical study of partial oxidation of a single coal particle in a stream of air. In: 2010 14th international heat transfer conference; 2010: American Society of Mechanical Engineers.
33. Safronov D, Kestel M, Nikrityuk P, Meyer B. Particle resolved simulations of carbon oxidation in a laminar flow. Can J Chem Eng. 2014;92(10):1669–86.

34. Zhao X, Jin H. Investigation of hydrogen diffusion in supercritical water: a molecular dynamics simulation study. Int J Heat Mass Transf. 2019;133:718–28.
35. Coetzee GH, Sakurovs R, Neomagus HWJP, Morpeth L, Everson RC, Mathews JP, et al. Pore development during gasification of South African inertinite-rich chars evaluated using small angle X-ray scattering. Carbon. 2015;95:250–60. https://doi.org/10.1016/j.carbon.2015.08.030.
36. Feng B, Bhatia SK. Variation of the pore structure of coal chars during gasification. Carbon. 2003;41(3):507–23.
37. Sadhukhan AK, Gupta P, Saha RK. Characterization of porous structure of coal char from a single devolatilized coal particle: coal combustion in a fluidized bed. Fuel Process Technol. 2009;90(5):692–700. https://doi.org/10.1016/j.fuproc.2008.12.010.
38. Jin H, Fan C, Wei W, Zhang D, Sun J, Cao C. Evolution of pore structure and produced gases of Zhundong coal particle during gasification in supercritical water. J Supercrit Fluids. 2018;136:102–9.